# Preliminary Soot Computations Based on a Model Aircraft Combustor With OpenNCC

**Manthena S. Raju**
**Manthena.s.raju@nasa.gov**
Vantage Partners, LLC (NASA GRC GESS-3)
3000 Aerospace Parkway
Brook Park, Ohio-44132
USA


**Jeffrey P. Moder and Changju T. Wey**
NASA Glenn Research Center
21000 Brook Park Road
Cleveland, Ohio-44135
USA

## ABSTRACT

In a preliminary effort to extend our current capabilities used in the design & testing of aero-engine combustors to particulate emissions, we incorporated several existing 2-equation soot models into the Open National Combustion Code (OpenNCC). The paper presents results from a validation study based on a well-characterized, swirl-stabilized, turbulent sooting flame generated by a model aero-engine combustor developed at DLR, Germany. The calculations are based on a Reynolds-Averaged Navier Stokes (RANS) simulation with standard k-ε turbulence model & a finite-rate chemical kinetic mechanism. A separate transport equation is solved for all individual species involved in ethylene/air combustion. The predicted velocity and temperature are mostly in good agreement with the measured data and reasonable agreement was found for soot. While the calculated SVF (Soot Volume Fraction) behavior is similar to some other predicted results reported in literature, the measured soot lasts farther downstream than the calculated soot indicating a need for further improvement in the soot models employed.

**Keywords:** Combustion, Emissions, CFD

## 1.0 INTRODUCTION

From an environmental perspective, soot and its precursors are suspected to be carcinogenic and there is a growing concern on their impact on climate modifications due to subsonic aircraft exhaust. Aside from the environmental concerns, there is a need to suppress soot formation as it represents incomplete & inefficient combustion from an engineering standpoint [1]. Also, the high radiative emissivity generated by soot may contribute to the formation of undesirable hot spots on the combustor walls [1]. In order to address various environmental & engineering concerns arising from the generation of emissions by jet engines, we developed a road map for soot modeling to be performed as part of the OpenNCC development.

The soot models can be broadly classified into two groups. The simple soot models are based on the nucleation of a single characteristic pyrolysis product, acetylene [5-6]. In more complex models, benzene, naphthalene, and/or pyrene are used as incipient species [1]. Also, they take into account the slow chemistry associated with Polycyclic Aromatic Hydrocarbons (PAH) [1, 7-10]. In addition to various models employed for nucleation, agglomeration, and oxidation, the soot models can be further sub-divided into three groups based on how the soot particle size distribution is evaluated [1, 5-10].

- Fairweather et al [5] developed a 2-equation model based on the solution of soot mass fraction ($Y_s$) and soot particle density ($N$). More on the models used for soot nucleation, surface growth, and oxidation can be found in [5-7]. In this approach, the particle size may vary but it is assumed to be mono-disperse at a given point in space.

- The above approach does not take into account the bi-modal nature of a typical soot particle distribution which is supposedly comprise of some large and some small particles [8]. In order to address this aspect, several studies were undertaken based on the method of moments approach [8]. However, such an approach is proven to be useful in studies where there is some prior knowledge of the particle distribution.

- The multiple-bin size model of Wey et al [9] is likely to provide a better representation for all the moments involved in the particle size distribution. The application of this method was so far demonstrated in the calculation of aerosol emissions in a post-combustor environment based on a known soot particle distribution.

In our preliminary effort, we incorporated the following 2-equation soot models into OpenNCC: Fairweather et al [1992], & Liu et al [2003]. Even though our primary interest lies in the calculations involving aviation fuels, because of the complexity involved in the chemical kinetic mechanisms of such fuels, our initial effort was focused on gaining some experience based on ethylene/air flames whose soot properties are well documented [1, 6, 10-13]. Based on our literature survey, we identified the following two mechanisms to be appropriate for use in our CFD calculations involving complex combustor configurations: a reduced mechanism based on 64-steps and 24-species of Kennedy et al [6], & a 210-steps and 32-species mechanism by Lu et al [11]. Both the reaction schemes contain a fuel breakdown step for the formation of acetylene, and steps needed to describe the destruction of this pyrolysis intermediate [5].

The experimental data available in literature for validation purposes is extensive. The most widely used source for experimental data is the website hosted by ISF (International Sooting Flame) Workshop. Because of our interest in aircraft engines, we selected what is identified to be the ISF-3 Target Flame 1 for which the experimental data was provided by KP Geigle of DLR, Germany [1]. It is a RQL (Rich-burn Quick-quench Lean-burn) combustor configuration. Both the CAD files needed for grid generation and the experimental data needed for validation were provided by DLR under a signed agreement. Further details of this combustor can be found in the results section. In this paper, we describe our computational experience based on the 2-equation soot models of [5] & [7], the gas-phase chemical kinetic mechanism of [6], & the experimental data of [1].

## 2.0 DETAILS OF SOOT MODELS IMPLEMENTED INTO OPENNCC

We first provide some details of the soot model developed by Fairweather et al [5]. The conservation equations for soot mass fraction, $y_{c(s)}$, and soot number density, $N$, are given as

$$[\rho y_{c(s)}]_{,t} + [\rho u_i y_{c(s)}]_{,x_i} - [\rho D y_{c(s),x_i}]_{,x_i} =$$
$$S_{c(s)} = r_1 M_{c(s)} + r_2 \rho M_{c(s)}{}^{1/3} y_{c(s)}{}^{2/3} N^{1/3}$$
$$-r_3 \rho M_{c(s)}{}^{1/3} y_{c(s)}{}^{2/3} N^{1/3}, \tag{1}$$

where $S_{c(s)}$ represents the instantaneous rate of formation of soot, and the terms on the right-hand side represent processes associated with nucleation, surface growth, and oxidation, respectively.

$$[\rho N]_{,t} + [\rho u_i N]_{,x_i} - [\rho D N, x_i]_{,x_i} =$$
$$S_N = r_4 - r_5 \rho^2 M_{c(s)}{}^{-1/6} y_{c(s)}{}^{1/6} N^{11/6}, \tag{2}$$

where $S_N$ represents the instantaneous rate of formation of $N$ per unit volume, and the terms on the right-hand side represent nucleation and coagulation, respectively. In Eq. 1,

$$r_1 = k_1 [C_2 H_2] \tag{3}$$
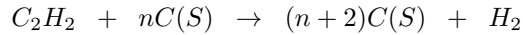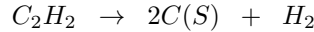$$r_2 = k_2 f(p) [C_2 H_2] \tag{4}$$

$$r_3 = k_3 f'(p) [O_2] \tag{5}$$

where

$$f(p) = \pi \left[\frac{6 M_{c(s)}}{\pi \rho_{c(s)}}\right]^{2/3} \tag{6}$$

$$f'(p) = f(p)/M_{c(s)}, \tag{7}$$

where $f(p)$ represents the functional dependence of surface area on the rate of soot formation due to surface growth. In this case it is assumed to be linear.

It is also important to note that the rates of nucleation and surface growth are determined based on the reaction steps given by

$$C_2 H_2 \;\; \rightarrow \;\; 2C(S) \;\; + \;\; H_2$$

$$C_2 H_2 \;\; + \;\; nC(S) \;\; \rightarrow \;\; (n+2)C(S) \;\; + \;\; H_2$$

and the reaction of soot oxidation is primarily assumed to proceed through

$$0.5 O_2 \;\; + \;\; C(S) \rightarrow \;\; CO$$

In Eq. 2,

$$r_4 = \frac{2}{C_{min}} N_A r_1 \tag{8}$$

$$r_5 = 2 C_a \left[\frac{6 M_{c(s)}}{\pi \rho_{c(s)}}\right]^{1/6} \left[\frac{6 k T}{\rho_{c(s)}}\right]^{1/2}, \tag{9}$$

Table 1. Rate constants as $AT^b e^{-E/RT}$.

| Rate constant | $A$ | $b$ | $E$ |
|---|---|---|---|
| $k_1$ | 1.35e+06 | 0.0 | 41e+03 |
| $k_2$ | 5.00e+02 | 0.0 | 24e+03 |
| $k_3$ | 1.78e+04 | 0.5 | 39e+03 |

In the above expressions, $M_{c(s)}$ is the molecular weight of soot (taken to be 12 kg/kmol), $N_A$ is the Avogadro number (6.022e+26 particles/kmol), $\rho_{c(s)}$ is the soot density (2000 kg/$m^3$), $C_{min}$ is the number of atoms in an incipient carbon particle (9000), $C_a$ is an agglomeration rate constant (3), $k$ is the Boltzmann constant (1.381e-23 J/K), and the rate constants, $k_i$, are given in Table 1.

In subsequent papers, e.g. Liu et al [7] & Kennedy et al [6], stressed the importance of including $OH$ radical in the soot oxidation mechanism. In Liu et al [7], the reaction steps involved in the soot oxidation are given by

$$0.5 O_2 \; + \; C(S) \rightarrow \; CO$$

$$OH \; + \; C(S) \rightarrow \; CO \; + \; H$$
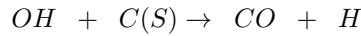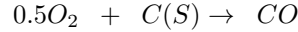
In Liu's model, the rate of soot oxidation in Eq. 5 is replaced by

$$r_{31} \; = \; 120[\frac{k_A[OH]\chi}{1 + k_Z[O_2]} + k_B[O_2](1 - \chi)]f_{O_2},$$

$$\chi \; = \; (1 + \frac{k_T}{k_B[O_2]})^{-1} \tag{10}$$

$$r_{32} \; = \; \phi_{OH} k_4(T) T^{-1/2}[OH] f_{OH} \tag{11}$$

where $\phi_{OH}$ represents the collision efficiency between the $OH$ radical and soot particles (0.1-0.13), the rate constants, $k_A, k_Z, k_B, \& k_T$, are taken from a paper by Fenimore et al [16], and $f_{O_2} \& f_{OH}$ represent functional                    dependence                    on                    temperature.

In addition to making some changes to $k_1$ and $k_2$, Liu et al [7] also reduced the value used for $c_{min}$ from 9000 to 700. This was done mainly to yield an inception soot particle diameter of 2.4nm. Kennedy et al [6] also increased the rate constant, $k_2$, used in the evaluation of surface growth by a factor of 2.
It is also important to note that in Eqs. (1) & (2), Fairweather et al [5] calculated the turbulent diffusion constant, $D$, as given by

$$D \; = \; \mu_t/\sigma_t \tag{12}$$

where $\mu_t$ = turbulent viscosity & $\sigma_t$ = turbulent Prandtl number. However, most soot calculations [6-7] stressed the importance of including the effect of thermophoresis on particle velocity based on an expression used in free molecular aerosol calculations. In Eqs. (1) & (2), they are replaced by

$$D y_{c(s),x_i} \; = \; -0.55 \frac{\mu_t}{\sigma_t T} T_{x_i} y_{c(s)} \tag{13}$$

$$DN, x_i \; = \; -0.55 \frac{\mu_t}{\sigma_t T} T_{x_i} N \tag{14}$$

## 3.0 THE CHEMICAL MECHANISM OF KENNEDY et al [6]

The chemical kinetic mechanism of Kennedy at al [6] is composed of 64 reactions & 24 species. It is based on a concise description of both $C_1$ and $C_2$ reactions encountered in ethene oxidation. It includes $C_1$ chemistry based on the methane mechanism developed by Smooke et al [12]. This mechanism contains enough detail to describe methane oxidation encountered in a laminar diffusion flame. The $C_2$ chemistry was described by a series of steps that convert $C_2H_4$ to $C_2H_3$ and $C_2H_2$. The intermediate steps needed for this conversion was based on Frenklach et al [13]. It also includes all the reactions deemed important in the formation and consumption of both $C_2H_3$ and $C_2H_2$ in alkyne diffusion flames based on Leung and Lindstedt [14].

When we first tried to run a reacting calculation based on the ISF-3 co-flow 1 of the ISF workshop [15], we ran into several numerical issues. However, the source of this problem was traced back due to a discrepancy found in the following two steps:

$H2 + M <=> H + H + M \quad 2.23E + 12 \quad 5 \quad 92600.$
$O2 + M <=> O + O + M \quad 1.85E + 11 \quad 5 \quad 95560.$
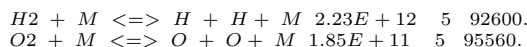
The above two steps in [6] were based on the methane mechanism developed by Smooke et al [12]. We were able to resolve this discrepancy by replacing the temperature exponents of the Arrhenius equation, $A\,T^b\,e^{-E/RT}$, by the following steps taken from [12]

$H2 + M <=> H + H + M \quad 2.23E + 12 \quad 0.5 \quad 92600.$
$O2 + M <=> O + O + M \quad 1.85E + 11 \quad 0.5 \quad 95560.$
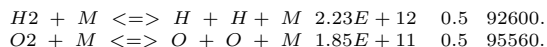
## 4.0 RESULTS & DISCUSSION

We provide some validation results based on the CAD files and experimental data that we received from DLR, Germany. It is for a RQL-type gas-turbine model combustor. Further details of this combustor can be found in several papers, e.g. [1].

### 4.1 Burner Configuration

The layout of the DLR model combustor is shown in Fig. 1. The combustor is 120 mm long with a square cross section of 68 x 68 mm$^2$. The burner, which is located at the bottom, comprises of three concentric nozzles. The primary air is supplied by means of two different nozzles: central and annular. The air though these nozzles is fed by separate radial swirlers. The central-air swirler has 14 channel openings and the ring-air swirler has 8. The gaseous fuel (ethylene) is injected in between the two air streams by means of 60 strait channels arranged in a narrow concentric ring. This fuel arrangement is designed in such a way that it mimics the atomizing lip of a liquid spray. Also, some secondary air is supplied to the combustor by means of cylindrical posts located at the four corners of the combustor. The secondary air is fed through the 5mm injector holes which are located at 80mm from the bottom of the combustor test section. Finally, the exhaust is removed though a circular duct located at the top of the combustion chamber.

### 4.2 Details of the Computational Grid & CFD Models

A 3D perspective view of the surface domain of the grid is shown in Fig. 2. The calculations were performed on an unstructured mesh with about 12.2 million computational cells. The computational mesh only covers certain portions of the combustor layout shown in Fig. 1. The central air enters the computational domain through the channel openings of the bottom swirler, the ring air enters through the channel openings of the swirler located above, and the secondary air enters directly through the holes located on the corners of the combustor. The flow patterns of the central, ring, and secondary airs can be better visualized by means of the $xy$ sectional views of the oxygen contours shown in Fig. 2. The gaseous ethylene fuel is injected in the middle of the gap located between the central and ring airs.
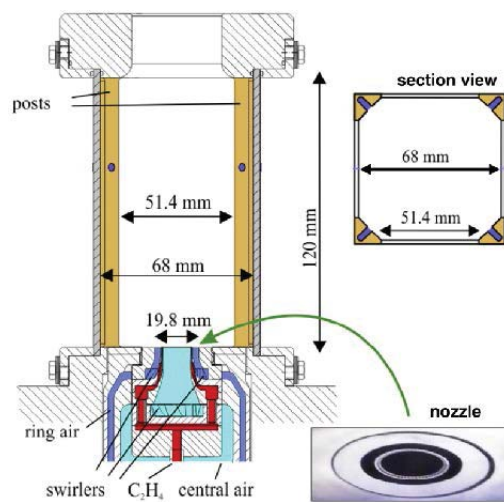
**Fig. 1  A cross-sectional layout of DLR model combustor (courtesy of Venkat Raman, Univ. of Michigan).**
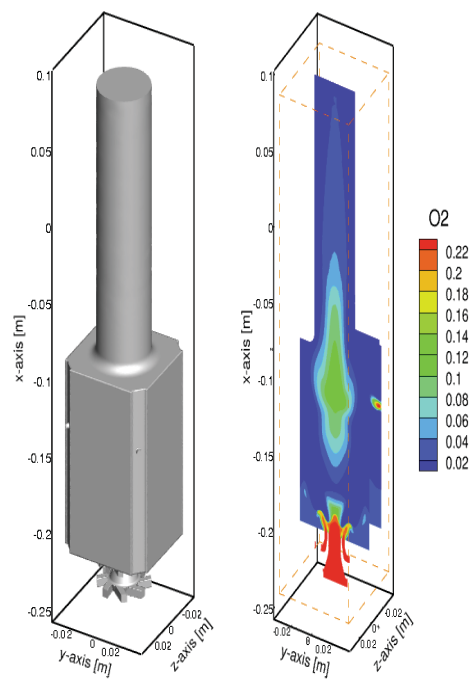


**Fig. 2  A 3D perspective view of computational domain & sectional views of $O_2$ contours in a reacting flow.**

The gas-phase computations are based on OpenNCC RANS with standard two-equation turbulence model, the gas-phase reduced chemical kinetics mechanism of Kennedy et al [6], & the 2-equation soot model of Fairweather et al [5]. The gas-phase computations are performed based on a central-differencing scheme with second-order accurate discretization for both viscous and inviscid fluxes. It makes use of a Jameson operator based on a blend of second and fourth-order artificial dissipation terms to achieve numerical stability. The steady-state RANS solution is obtained by making use of an explicit, four-stage Runge-Kutta scheme. The convergence to steady-state is accelerated by making use of residual smoothing of residuals in pseudo time. It is noteworthy that no attempt was made in these calculations to include any chemistry-turbulence interaction models.

### 4.3 Initial Test Conditions

For this combustor, detailed velocity & SVF data were reported over a wide range of operating conditions [1]. Also, some limited temperature data was reported. In particular, starting from a reference point of 3 bar and a thermal power of 30 $KW$, the influence of secondary air, thermal power, split between central and ring air, and equivalence ratio on soot formation were investigated [1]. In this paper, we present results from two different calculations based on the following input conditions:

1. Pressure, 3 bar; mass flow rates for ring, central, & secondary air, 7.08, 3.03, & 4.04 g/s, respectively; fuel mass flow rate, 0.83 g/s; air temperature, 297 deg. K; & fuel temperature, 293 deg. K. The resulting global equivalence ratio is 0.86.

2. All other conditions remain the same as above but without any secondary air. The corresponding global equivalence ratio is 1.2.

### 4.4 The Results From a Calculation With Secondary Air

The predicted contour plots of velocity & temperature are shown in Fig. 3. They represent the xy sectional views of the DLR combustor at $z = 0.0$, 0.015, & 0.0275. The magnitude of velocity ranges from -5 to 20 m/s and of temperature from 440 to 2200 deg. K. The u-velocity contours are shown at z = 0.0 but the contours at z = 0.015 & 0.0275 represent v-velocity. The u-velocity contours show that the flow is characterized mainly by a strong central swirl-induced primary recirculation region (toroidal vortex) and a corner vortex formed in the lower region of the combustor. The swirl effect on the the incoming air is evident with its direction being strongly deflected radially outwards. The incoming air is subjected to a strong shear as it moves through the middle of the two counter rotating vortices (primary & corner). Also, one can notice some attendant increase in gas velocity due to combustion where a flame is stabilized in the inner shear layer of the primary vortex.

The gas temperature at $z = 0.0$ is characterized by three distinct regions: a low temperature region associated with the incoming air, it is followed by a hot temperature region due to combustion, and a quench region formed further downstream due to the entrained secondary air. The heat losses at the walls are also clearly evident. Also, it is mostly hot gases that recirculate within the corner vortex.

One can gain a better understanding of how the secondary air is entrained into the middle of the quench region by following its movement from the successive sectional views starting from z = 0.0275 to 0.0. The secondary air enters from the four corners of combustor through the circular holes located at $x = 0.80$ near $z = 0.0275$. The diffusion effect on the entrained air is evident from the contours of both v-velocity and temperature at z = 0.015. Also, the cooling effect of the entrained air is evident from the temperature contours. Once the entrained air is drawn into the middle of the combustor, its interaction with the primary recirculation is such that it results in a flow pattern similar to that encountered in a stagnation-point flow generated by opposing flows. While part of the entrained air is drawn downstream by the motion of toroidal vortex, and the rest is drawn upstream towards the exhaust. As a result, the entrained air is subjected to a strain rate similar to that encountered in a stagnation-point flow. The
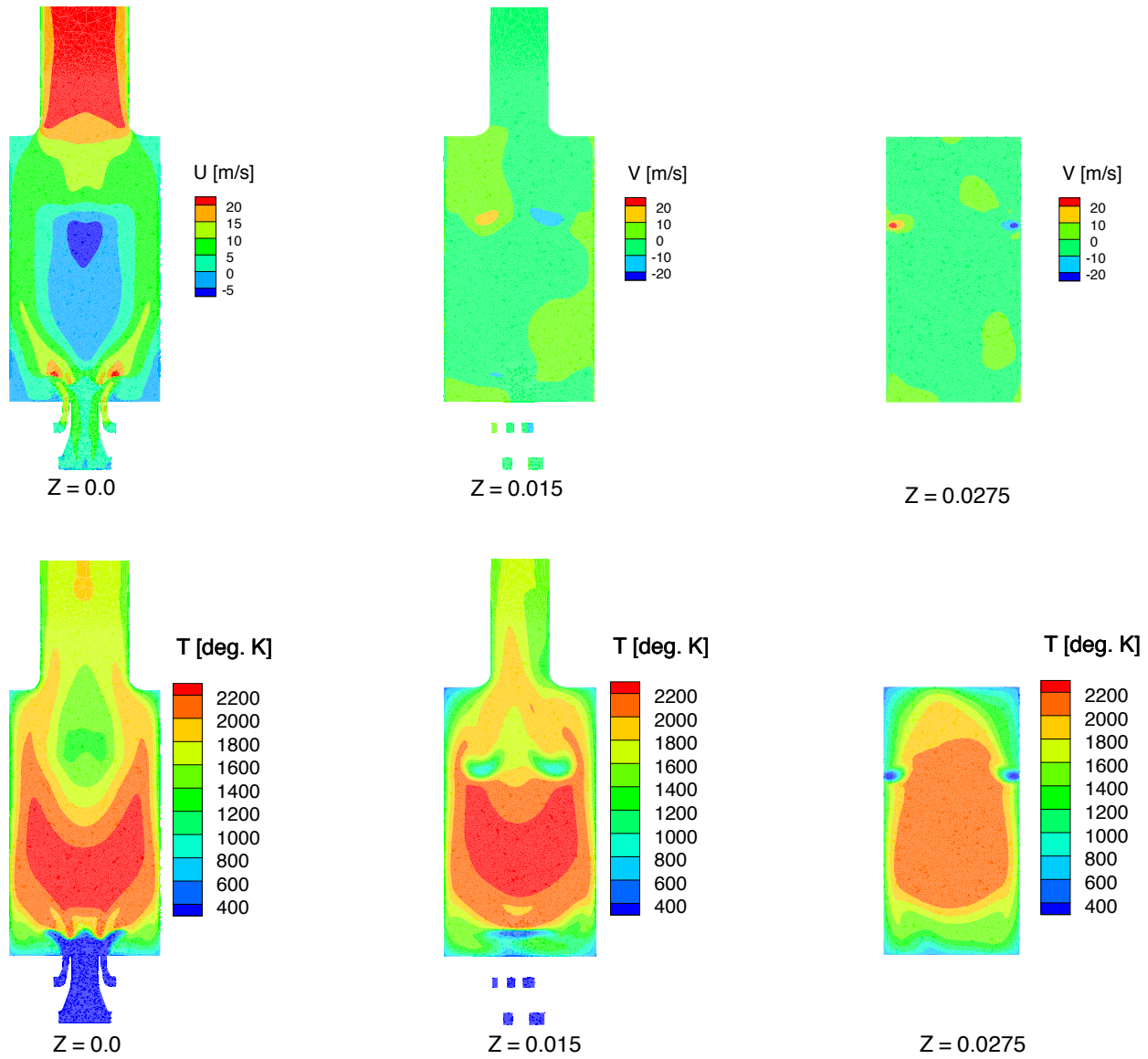
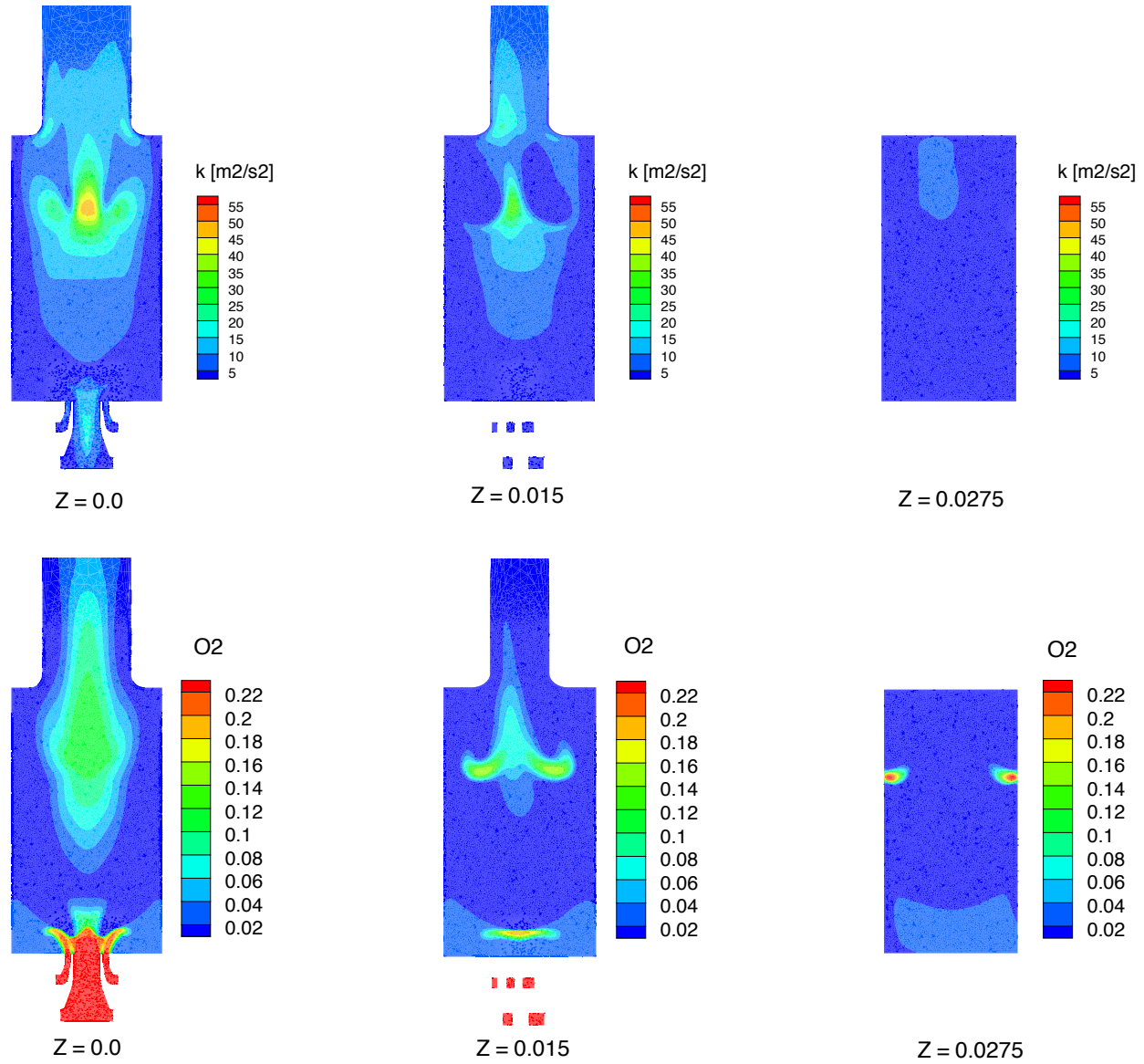Fig. 3 Sectional views of calculated velocities & temperature at different Z locations.

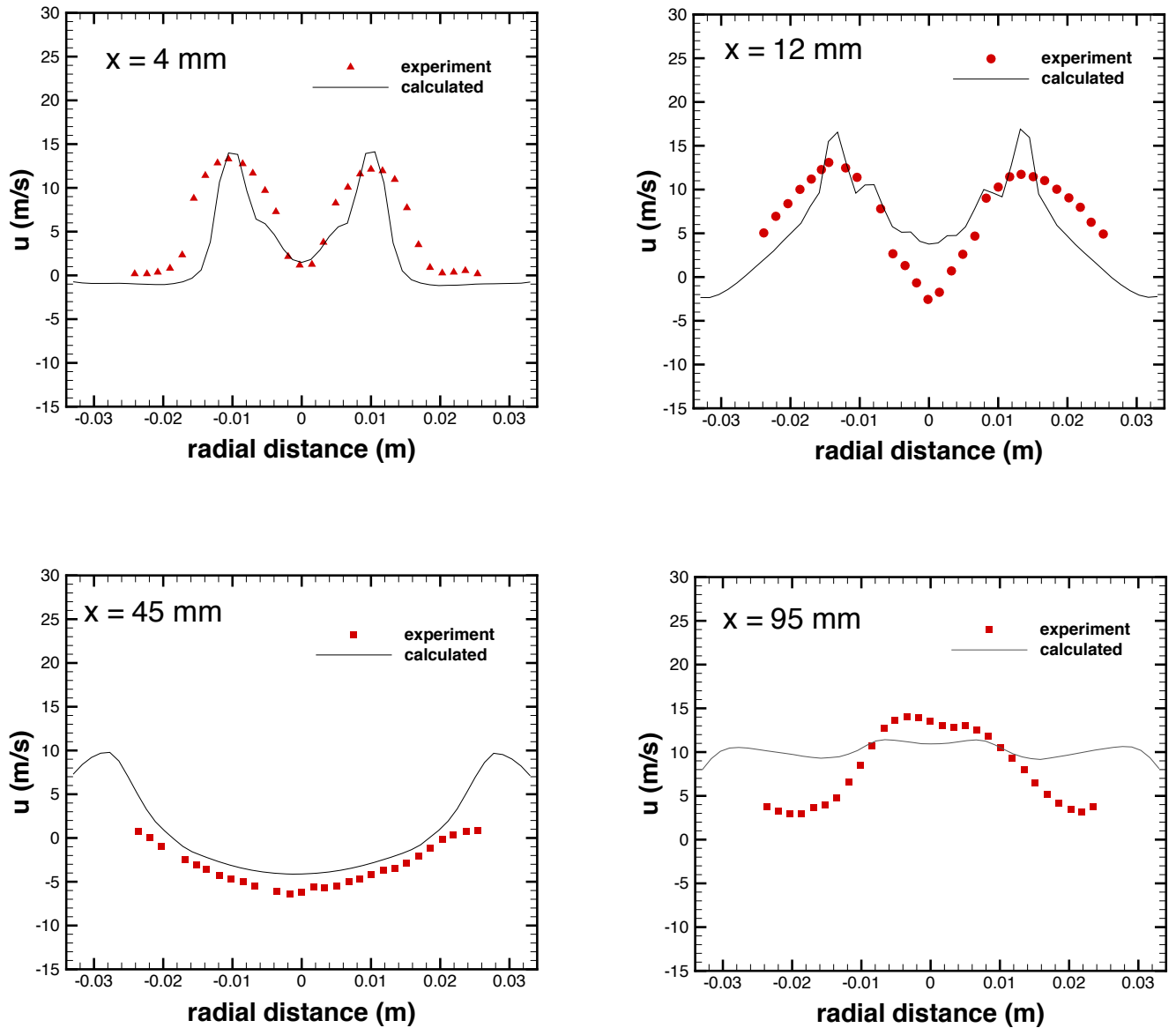Fig. 4 Sectional views of calculated $O_2$ & turbulent kinetic energy at different Z locations.

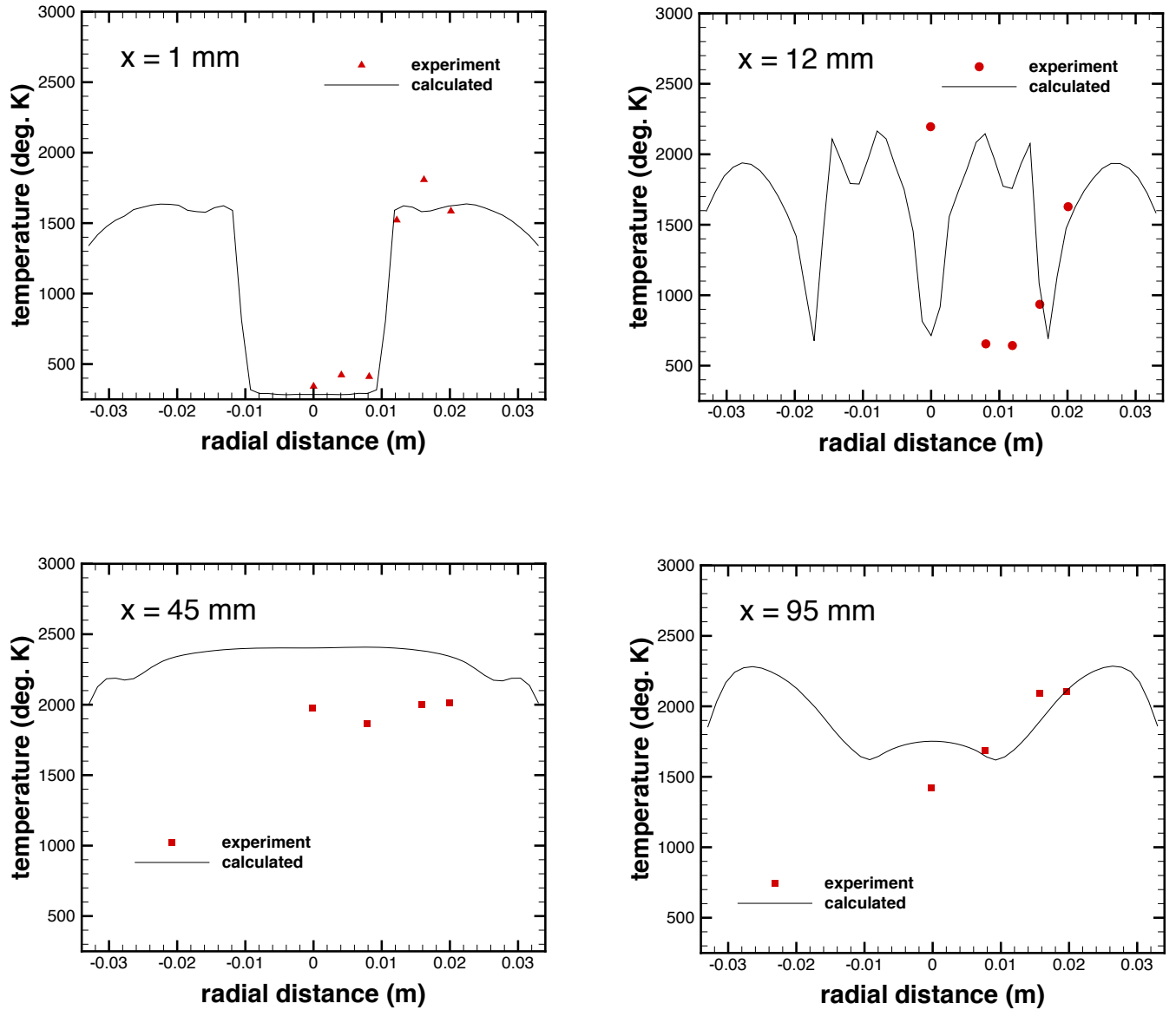Fig. 5 Axial velocity comparisons at selected downstream locations at Z = 0.

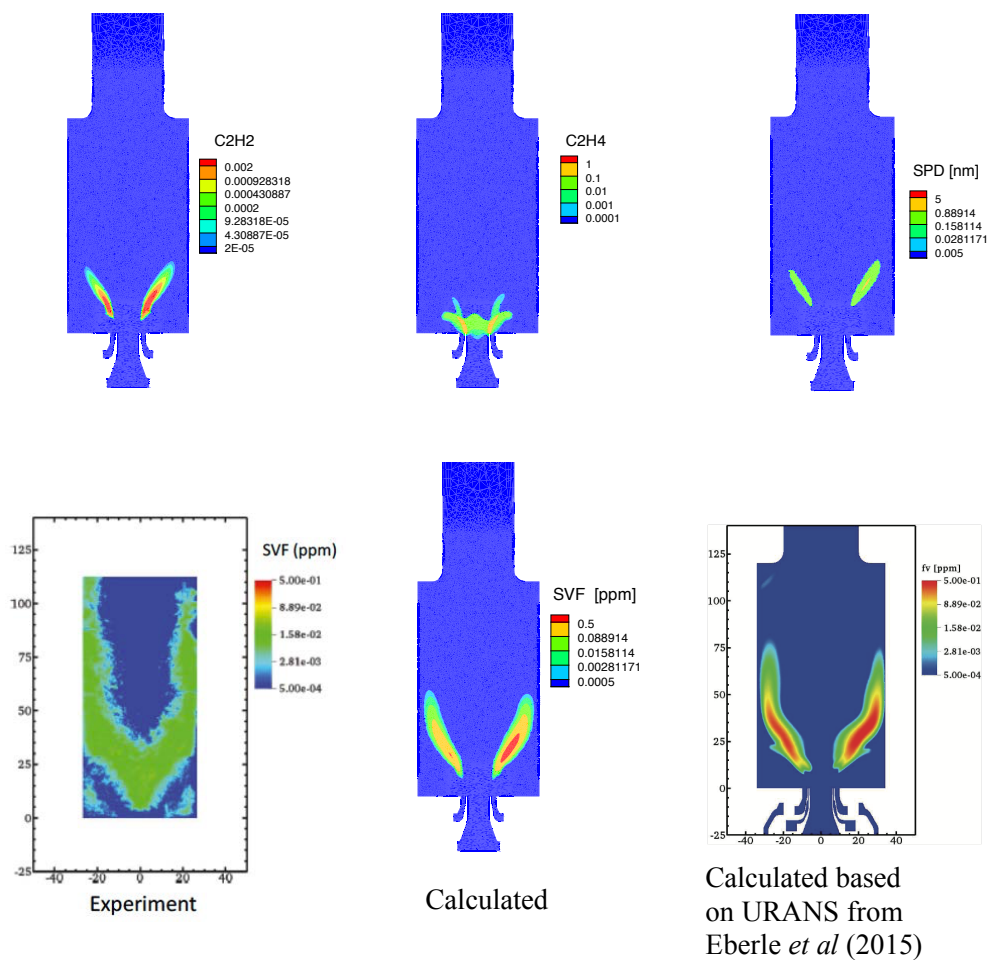Fig. 6 Temperature comparisons at selected downstream locations at Z = 0.

Fig. 7 Calculated plots of $C_2H_2$, $C_2H_4$, soot particle size, & measured and calculated soot volume fraction.

overall interaction of the entrained air with the primary recirculation seems to have two major consequences: (1) it helps to shift the toroidal vortex core location further downstream towards the quench region as evidenced by the location of the negative u-velocity region, & (2) it also enhances strain rate in that region as evidenced by the higher turbulence energy levels observed at $z = 0.0$ of Fig. 4. The diffusion effect on the entrained air is also evident from the corresponding oxygen contours shown in Fig. 4.

The u-velocity comparisons at selected downstream locations are shown in Fig. 5. These locations are chosen as they represent significant regions of the flame, the first two are from the inner region of the flame with steep gradients, the third from the post-combustion (primary) region, and the last from the post-quench region [1]. In the first two locations, the flow is characterized by two peaks formed between inner and outer shear layers and a significant recirculation in the middle [1]. While the locations of these peaks are well captured, the calculated peaks are less wider than the experiment in both locations. The calculation underpredicts the magnitude of both velocity peaks and also the negative velocity in the middle of primary recirculation at the second location. The homogenization of the velocity in the middle is well captured at the third location. Also, it is noteworthy that the experimental data does not extend to the walls to capture the peaks predicted near the walls. At the last location of the post-quench region, the calculations slightly underpredict the velocity in the center region. However, our calculation overpredicts the u-velocity by a considerable measure as it fails to resolve the upper corner region of the combustor. However, our predicted results could be improved considerably by refining the grid in this region.

The temperature comparisons are shown at selected downstream locations in Fig. 6. The temperature measurements are only reported for one half of the combustor cross section. There is a good comparison between the predicted and measured temperatures near the inflow at x = 1 mm. As expected, the temperature in the central region is close to near ambient temperature of the inflow air. Away from this region, there is a sharp rise in temperature as burnt gases mostly recirculate in the outer corner vortex. At the next location, there is a sharp rise in the measured temperature in the middle. However, our calculation shows a temperature raise to occur mostly within the low temperature region of the corresponding measured data. The disparity between the measured and predicted temperatures could be attributed to the differences observed in measured and calculated u-velocity comparisons. In both experiment and our calculation, the temperature starts to rise after a flame is stabilized in the inner shear layer. While the location of the velocity peaks is correctly predicted, our calculation underestimates the spread of velocity near its peak by a considerable measure. As a result in our calculations, a flame originating at a far away location near its velocity peak fails to reach all the way to the middle. However, the observed steep raise in measured temperature is a result of a flame originating much closer to the middle. The observed disparity between measured and predicted temperature behavior at this location could be improved by a better resolution of the grid in this region. At x = 45 mm, the temperature is mostly uniform at this post-combustion location. The calculated temperatures are about 100 deg. K higher than the experiment. Some of the discrepancy could be attributed to the losses generated by radiation. There seems to be mostly good agreement between the predicted and measured temperatures in the post-quench region at x = 95 mm.

The calculated plots of $C_2H_2$, $C_2H_4$, soot particle size, & measured and calculated plots of SVF are shown in Fig. 7. Also, shown in Fig. 7 is the the calculated plot of the SVF from Eberle et al [1]. It was obtained based on an Unsteady Reynolds-Averaged Navier-Stokes (URANS) solution. As described earlier, our calculations are based on the soot model of Fairweather et al [5]. However, it is noteworthy that the value used for $C_{min}$ was reduced from 9000 to 700 to yield an inception soot particle diameter of 2.4nm following the approach taken in several recent papers including Liu et al [7].

The mass fractions for acetylene & ethylene range between 0.0 to 0.004, & 0.0 to 1.0, respectively, and the soot particle diameter ranges between 0 to 5 nm. The acetylene is formed mostly within the inner region of the flame. One can notice slight asymmetry in our calculated acetylene distribution. The expected resulting asymmetry is also evident in our calculated SPD and SVF distributions.

There are three main differences between the measured and calculated SVF distributions: (1) Even though the selected range is between 0.5 to 0.0005, the reported maximum for measured SVF is only 0.035. Our calculated maximum is 0.74 and it is about 0.54 in the calculation of Eberle et al [1]. (2) In both calculations, most of our predicted soot vaporizes within 60 mm of the burning section. This is in contrast with the measured data where its is observed to last further downstream up to 100 mm. As described in [1], the reasons for rapid soot oxidation could partly be attributed to the overpredicted soot concentration levels. It is because the calculated oxidation rates are proportional to the soot concentration levels. Therefore, the overpredicted soot concentration levels lead to the soot precursor (such as acetylene) being consumed too quickly and hinders the formation of subsequent soot growth required to balance further soot oxidation downstream. (3) The measurements also show for the soot to form much closer to the injector in the central region. The discrepancy in our calculation could be attributed to the reasons we discussed earlier on the flame development in this region.

### 4.5 The Results From a Calculation With No Secondary Air

The predicted contour plots of u-velocity, kinetic energy, temperature, and the mass fractions of $O_2$, $C_2H_4$, & $C_2H_2$ are shown in Fig. 8. They represent the xy sectional views of the DLR combustor at $z = 0.0$. Since the global features of the flowfield were already described in considerable detail in the last section, here we highlight some major differences resulting from the lack (or use) of secondary air. From a comparison of the contour plots in Fig. 8 to those corresponding in Figs. 3, 4, & 7, the influence of secondary air is evident in a number of important ways: (1) Without any secondary air, the flow is characterized primarily by a strong swirl-induced primary recirculation and a corner vortex located in the lower region of the burning section. As descried in earlier, the entrained secondary air further strengthens the negative region of the primary recirculation in the downstream location. The expected increase in the exit velocity due to the addition of secondary air is clearly evident. (2) In both calculations, the high kinetic energy region is located downstream of the primary recirculation zone. The interaction of the secondary air with the toroidal vortex of the primary recirculation leads to an increased kinetic energy level in this region. More on the interaction can be found in the previous section. (3) Without the cooling effect of the secondary air, the high temperature region remains fairly uniform downstream. As described earlier, the entrained secondary air modifies the temperature region in several significant ways. (4) In both calculations, most of the oxygen from primary (ring and central) air is consumed by a flame stabilized in the inner region of primary recirculation. The interaction of the primary recirculation with the secondary air leads to a complex pattern of oxygen contours as seen in Fig. 4. (5) While the $C_2H_4$ contours are similar in both calculations, the $C_2H_2$ contours differ in significant ways. The increased oxygen levels associated with secondary air limits the formation of acetylene to a small region near the flame. Without secondary air, its concentration extends all the way to the middle without generating any void in the middle of downstream.

There is a good agreement in the axial and radial velocity comparisons shown in Fig. 9 at selected downstream locations at $Z = 0.0$. It is important to note that some minor oscillation continued to be present with the calculated primary primary recirculation region slightly moving back and forth in the axial direction. The predicted results could be further improved by refining the grid in this region. Also, there is a good agreement between the predicted and measured centerline temperatures shown in Fig. 10. As described earlier, most of the combustion takes place within 1 cm of the burning section. The gas temperature remains fairly uniform following combustion at about 2100 deg. K.

The measured and calculated plots of SVF are shown in Fig. 11. Also, shown are the predicted results based on LES from Raman et al [17] and the experimental results of Geigle et al from DLR [17]. The selected range for the SVF data is from 0 to 75 ppb. However, our calculated maximum is about 150 ppb. It is important to note that our results are based on a logarithmic scale and the other two are based on a linear scale.
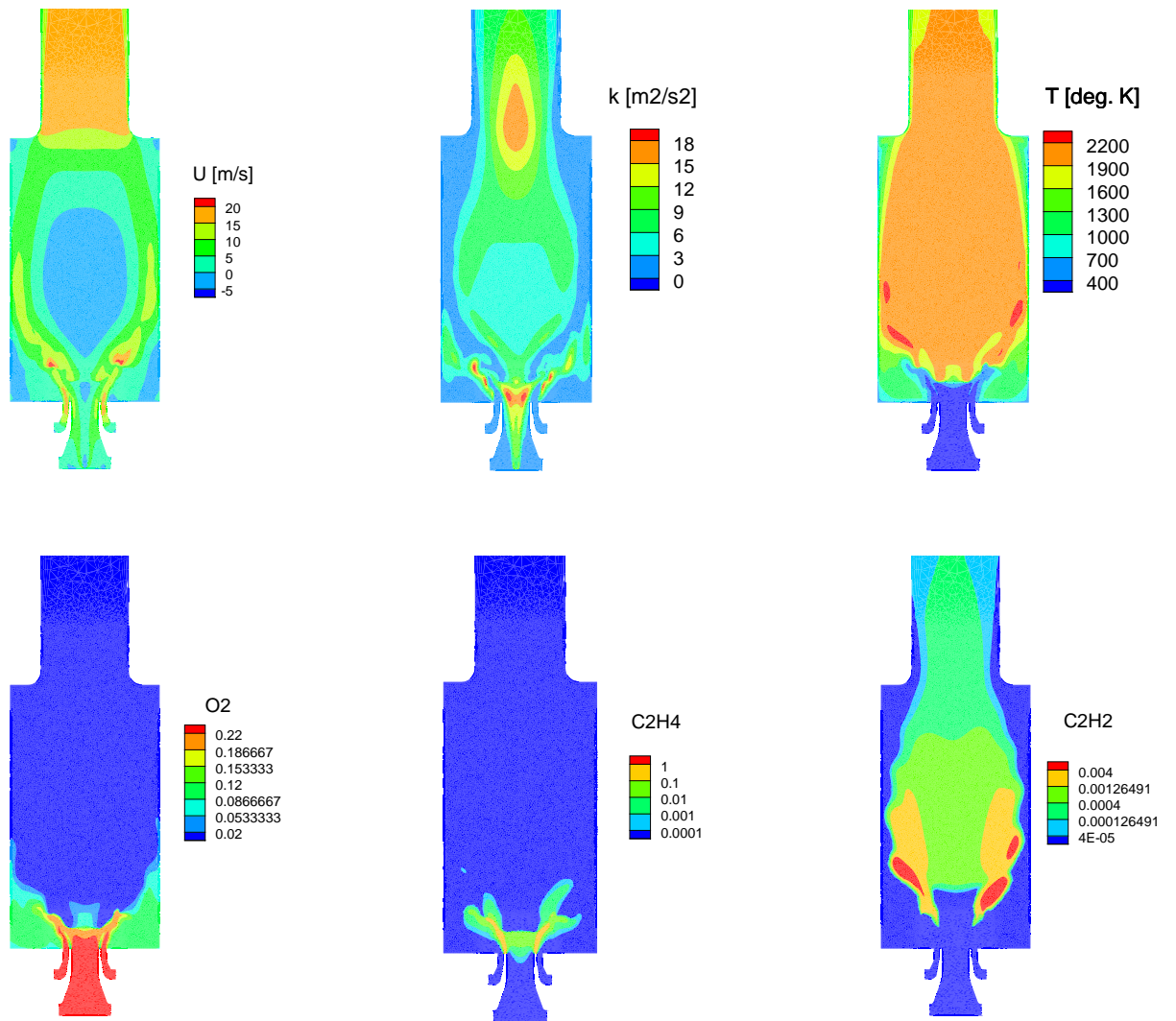
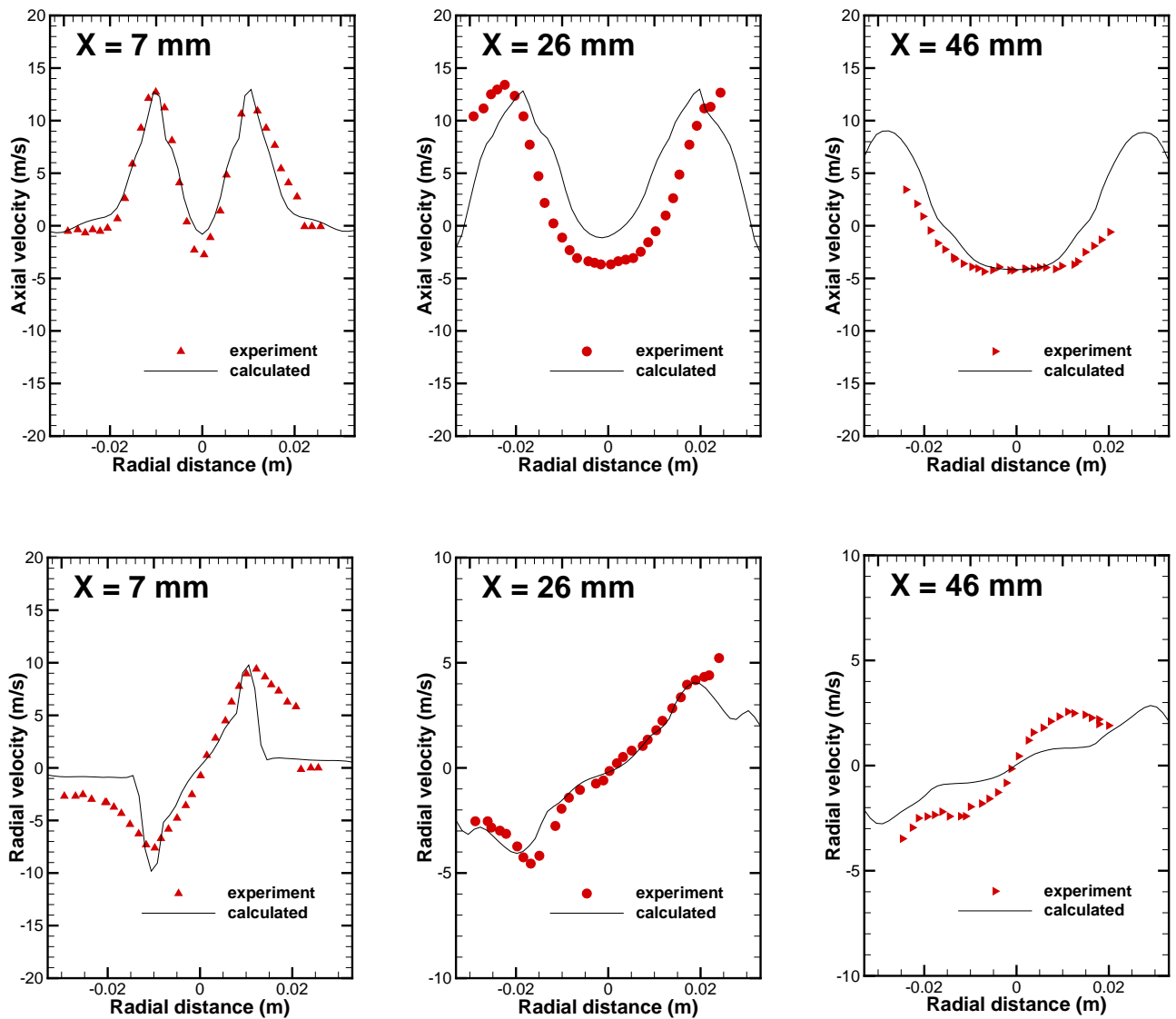Fig. 8 Sectional views of some predicted flow variables at Z = 0.0.

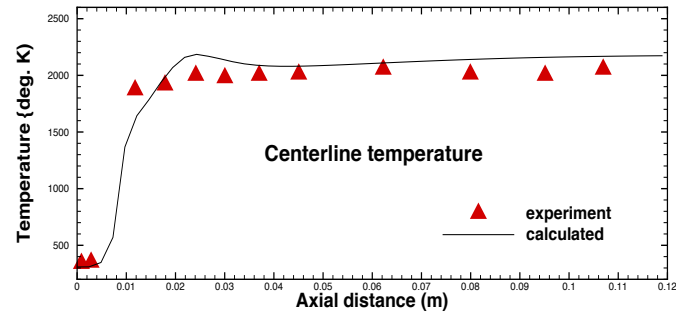Fig. 9 Axial & radial velocity comparisons at selected downstream locations at Z = 0.0.

Fig. 10 Centerline temperature comparisons in the burning section of combustor.



Calculated from          Experimental data          Calculated
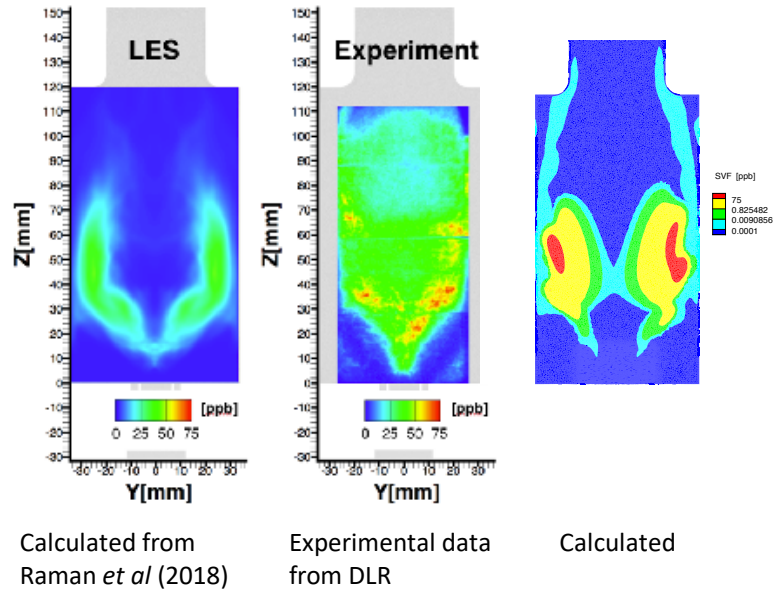Raman *et al* (2018)      from DLR

Fig. 11 Measured and calculated plots of soot volume fraction.

The experimental data shows for the soot to originate in the middle closer to the fuel injector. It then spreads radially outwards until it reaches the outer boundary. The high levels of soot concentration are observed to form slightly downstream of the interior to the boundary of soot formation. The measured soot is observed to last up to a downstream location of 110 mm before it oxidizes. Unlike what we observed with secondary air, the measured soot distribution extends all the way to the middle without developing a void in the middle of downstream.

Our calculations show for the high levels of soot concentration to occur downstream of the high acetylene region. Most of the soot is located in a small region of high soot concentration. Moreover the soot from this region quickly dissipates into a much lower level in the surrounding region. The reason for this behavior could partly be attributed to the rapid level of oxidation caused by the corresponding higher values of predicted soot concentration. Most of the predicted soot in our calculations vaporizes within 80 mm of the burning section.

The predicted pattern of soot concentration in [17] is qualitatively similar to what we observed earlier in our calculation with secondary air. The soot is mostly formed over a small band in the inner region of the primary recirculation [17]. After that it spreads further downstream near the outer wall before vaporizing completely at about 80 mm similar to what we observed in our calculation. The soot distribution is relatively uniform but the levels of soot concentration are much lower than the experiment. It is noteworthy that both the predicted results fail to predict the experimentally observed soot formation in the downstream locations past 80 mm. Unlike the experiment, both calculations show a void in the middle of the calculated downstream soot distribution. It is important to note that in our calculation the soot distribution is more non-uniform and the maximum level of soot concentration is slightly higher than the experiment.

## 5.0 CONCLUDING REMARKS

In an effort to aid our current gas-turbine combustor design & testing effort, we extended the Open-NCC code development to soot calculations by incorporating the soot models developed by [5] & [7]. As a part of this effort, we also undertook a validation study based on a well-characterized, confined, swirl-induced sooting flame generated by a model aero-engine combustor developed at DLR, Germany. The calculations were based a RANS solution with standard $k - \epsilon$ turbulence model and a separate transport equation is solved for all individual species. The results provided reasonable agreement with the reported experimental data on velocity and temperature. While our calculated SVF is similar to other predicted results of [1] & [17], our computational experience indicates a definite need for further refinement in the soot models employed. The predicted results could be improved by refining the grid in the inner central region of the burning section and near the corner vortex of the post-quenching region. Also, there is a need to incorporate a radiation model in our soot computations.

We are currently working on extending our calculations to aviation fuels by undertaking validation based on a partially-fueled 9-element LDI combustor. The measurements are based on the $CO$ & soot particle emissions testing performed in a combustion rig, CE-5, operated at NASA Glenn research center.

### REFERENCES

1. Eberle, C., Gerlinger, P., & Aigner, M., "A Comparison of URANS and LES For Soot Predictions in an Aero-Engine Model Combustor," Deutscher Luft- und Raumfahrtkongress 2015, DocumentID: 370050.

2. Liu, N.-S., Shih, T.-H., & Wey, C.T., "Comprehensive Combustion Modeling and Simulation: Recent Progress at NASA Glenn Research Center," ISABE-2007-1268, 18th International Symposium on Air Breathing Engines, Beijing, China, September 2-7, 2007.

3. Raju, M.S., "LSPRAY-V: A Lagrangian Spray Module," NASA/CR-2015-218918, NASA Glenn Research Center, Cleveland, Ohio, November, 2015.

4. M.S. Raju, "EUPDF-II - An Eulerian-Based Monte Carlo Probability Density Function (PDF) Solver - User's Manual," NASA/CR-2004-213073, NASA Lewis Research Center, Cleveland, Ohio.

5. Fairweather, M., Jones, W. P., and Lindstedt, R. P., "Predictions of Radiative Transfer from a Turbulent Reacting Jet in a Cross-Wind", Combustion & Flame, Vol. 89, 1992, pp. 45-63.

6. Kennedy, I.M., Yam, C., Rapp, D.C., & Santoro, R.J., "Modeling and Measurements of Soot and Species in a Laminar Diffusion Flame," Combustion and Flame, 107: 368-382 (1996).

7. Liu, Fengshan, Guo, Hongsheng, Smallwood, Gregory J, & Gulder, Omer, "Numerical modeling of soot formation and oxidation in laminar coflow non-smoking and smoking ethylene diffusion flames," Combustion Theory and Modeling, vol. 7, no. 2, pp. 301-315 (2003).

8. Mueller, M.E., Blanquart, G., & Pitsch, "Hybrid Method of Moments fro modeling Soot formation and Growth" Combustion and Flame, 156: 1143-1155, (2009)

9. Wey, T., & Liu, N.-S., "Modeling Jet Egine Aerosols in the Postcombustor Flow Path and Sampling System." J. of Propulsion and Power, 23: 930-941 (2007).

10. Seth B. Dworkin, Qingan Zhang, Murray J. Thomson, Nadezhda A. Slavinskaya, & Uwe Riedel, "Application of an Enhanced PAH Growth Model to Soot Formation in a Laminar Coflow Ethylene/Air Diffusion Flame", Combustion and Flame, 158: 1682-1695, (2011).

11. Lu, T., & Law, C.K., Proc. Combt. Inst., 30: 1333-1341, (2005).

12. Smooke, M.D., Puri, I.K., & Seshadri, "A Comparison between Numerical Calculations and Experimental Measurements of the Structure of a Counterflow Diffusion Flame Burning Diluted Methane in Diluted Air," Twenty-first Symposium (International) on Combustion/The Combustion Institute, pp. l783-1792, 1986.

13. Frenklach, M., Wang, H., and Rabinowitz, M. J., Progress in Energy and Combustion Science, 18:47-73 (1992).

14. Leung, K. M., and Lindstedt, R. P., Combust. Flame, 102:125-160 (1995).

15. Santoro, R.J., Semerjian, H.G., & Dobbins, R.A., "Soot Particle Measurements in Diffusion Flames" Combustion & Flame, 51: 2003-218, 1983.

16. Fenimore, C.P. and Jones, G.W., J. Phys. Chem. 71: 593-597, 1967.

17. Raman, V., Mueller, M., & Anand, M.S., "Fuel Sensitive Models for Predicting Flame Stability and Emissions from Aircraft Combustors," NASA Review 2018.